Cubic spline solver for generalized density functional treatments of atoms and generation of atomic datasets for use with exchange-correlation functionals including meta-GGA

N. A. W. Holzwarth [1], Marc Torrent [2], Jean-Baptiste Charraud,[2] and Michel Côté [3]
[1]*Department of Physics, Wake Forest University, Winston-Salem, North Carolina 27109, USA*
[2]*CEA, DAM, DIF, F91297 Arpajon, and Université Paris-Saclay, CEA, Laboratoire Matière en Conditions Extrêmes, 91680 Bruyères-le-Châtel, France*
[3]*Département de Physique, Université de Montréal, C.P. 6128, Succursale Centre-Ville, Montréal, Canada, H3C 3J7*

(Received 17 December 2021; revised 8 March 2022; accepted 9 March 2022; published 31 March 2022)

Within generalized density functional theory, recent developments of functionals which depend upon the kinetic energy density, such as the r2SCAN form, show significant improvement in the computational representation of real material properties. In order to implement these forms within plane-wave codes, it is necessary to use pseudopotentials, ideally constructed with the same exchange-correlation functional as has been implemented for the projector augmented-wave (PAW) formalism in the ATOMPAW code. This was accomplished with the help of an efficient solver for the self-consistent radial bound states of each atom, based on cubic spline interpolation. Details of the formalism are presented, and preliminary results for several simple materials are encouraging.

DOI: 10.1103/PhysRevB.105.125144

I. INTRODUCTION

There have been many new developments in density functional theory [1,2], including semilocal components treated within a generalized Kohn-Sham approach [3]. For example, the meta-GGA SCAN functional recently proposed by Sun *et al.* [4] shows a lot of promise for representing material properties [5–13]. Despite a lot of successes of the SCAN functional, it has been noted that the original SCAN formulation has some numerical issues [6,14]. Recently, a r2SCAN functional has been proposed [15] to improve the numerical performance of the SCAN functional while also maintaining most of the physical constraints used in the design of the original SCAN functional. This work, together with many other meta-GGA functionals found in the literature, suggest that the meta-GGA functionals are likely to be important tools for materials simulations. Some of the details of the meta-GGA formalism within the context of the generalized Kohn-Sham approach [3] have been presented in the literature by Sun *et al.* [16] and by Yao and Kanai [17].

Throughout the long history of pseudopotential methodology, it is the usual practice to construct the pseudopotential data sets with the same exchange-correlation functional that will be used for materials simulations. However, for the meta-GGA studies, it is frequently the case that pseudopotential data sets constructed with other exchange-correlation functionals are used, as explained, for example, in Ref. [12]. In the present work we develop a self-consistent solver for the generalized Kohn-Sham equations for spherical atoms and adapt the projector augmented-wave (PAW) method of Blöchl [18] in order to construct PAW datasets for atoms throughout the periodic table for use with these meta-GGA functionals. The resulting code is implemented in the ATOMPAW [19] software package with the expectation that they can be used with general-purpose plane-wave density functional codes such as ABINIT [20] and QUANTUM ESPRESSO [21].

The outline of this paper is as follows. Section II presents the formalism for solving the all-electron generalized density functional equations for spherical atoms. Numerical challenges of solving for the radial wave functions are noted and the spline interpolations solver method is presented with details given in Appendix A. Section III discusses the PAW formalism [18], particularly with a view of modifications needed for solving the generalized Kohn-Sham equations with meta-GGA exchange-correlation contributions. Some additional details are given in Appendix B. A few of the constructed PAW datasets are used to analyze binding energy curves of some simple solids using the meta-GGA enabled [22] version of ABINIT. A summary and conclusions are presented in Sec. V. Sample input data for ATOMPAW and ABINIT are available in the Supplemental Materials [23].

II. FORMULATION AND APPLICATION TO SPHERICAL ATOMS

A. Formalism

1. Total energy for density functional theory

Density-functional-theory calculations start with the total (electronic) energy of the system in terms of the kinetic ($E_{\rm kin}$), electron-nucleus (E_{eN}), electrostatic electron-electron or Hartree (E_H), and exchange-correlation (E_{xc}) contributions:

$$E_{\rm tot} = E_{\rm kin} + E_{eN} + E_H + E_{xc}. \tag{1}$$

In practice we assume that our system has occupied Kohn-Sham orbitals $\Phi_i(\mathbf{r})$ with occupancy factors w_i; then the

electron density is given by

$$n(\mathbf{r}) = \sum_i w_i |\Phi_i(\mathbf{r})|^2. \tag{2}$$

The kinetic energy of the system can also be calculated in terms of the occupied Kohn-Sham orbitals and the corresponding kinetic energy density $\tau(\mathbf{r})$ according to

$$E_{\rm kin} = \int d^3r\ \tau(\mathbf{r}) \quad \text{where} \quad \tau(\mathbf{r}) = \frac{\hbar^2}{2m}\sum_i w_i |\nabla\Phi_i(\mathbf{r})|^2. \tag{3}$$

The electron-nuclear and Hartree energies are given by

$$E_{eN} = \int d^3r V_N(\mathbf{r}) n(\mathbf{r}), \tag{4}$$

and

$$E_H = \frac{e^2}{2}\int d^3r \int d^3r' \frac{n(\mathbf{r})n(\mathbf{r}')}{|\mathbf{r}-\mathbf{r}'|}. \tag{5}$$

Here $V_N(\mathbf{r})$ denotes the electron-nuclear potential $(-e^2Z/r)$ for a single atom of atomic number Z and e denotes the elementary charge.

2. Exchange-correlation formulations and generalized Kohn-Sham equations

In order to discuss exchange-correlation formulations, it is convenient to use the notation developed by the LIBXC library software [24,25]. For simplicity, in this work we do not consider spin polarization [26]. The following functional form for the exchange-correlation energy can be analyzed [27]:

$$E_{xc} = \int d^3r\ f_{xc}\big(n, \sigma, \nabla^2 n, \tau\big). \tag{6}$$

Exchange-correlation functionals that only depend on $n(\mathbf{r})$ are categorized as local density approximation (LDA) treatments. The next level of treatment involves inclusion of the gradient of the density at the so-called generalized gradient approximation (GGA), which can be represented by σ:

$$\sigma \equiv |\nabla n|^2. \tag{7}$$

The meta-GGA (MGGA) level of the treatment involves the Laplacian of the density ($\nabla^2 n$) and/or the kinetic energy density $\tau(\mathbf{r})$ defined in Eq. (3).

These contributions affect the effective exchange-correlation functional within the generalized Kohn-Sham equations with the form

$$V_{xc}(\mathbf{r}) = \frac{\partial f_{xc}}{\partial n} - \nabla\cdot\left(2\frac{\partial f_{xc}}{\partial\sigma}\nabla n\right) + \nabla^2\left(\frac{\partial f_{xc}}{\partial(\nabla^2 n)}\right). \tag{8}$$

Additionally, the kinetic energy density $[\tau(\mathbf{r})]$ contribution enters the generalized Kohn-Sham equations in terms of a dimensionless "kinetic potential" $V_\tau(\mathbf{r})$, defined in terms of the functional derivative

$$V_\tau(\mathbf{r}) = \frac{\partial f_{xc}}{\partial\tau}. \tag{9}$$

The corresponding generalized Kohn-Sham equations are given by

$$H(\mathbf{r})\Phi_i(\mathbf{r}) = \varepsilon_i\Phi_i(\mathbf{r}), \tag{10}$$

where

$$H(\mathbf{r}) \equiv \left(-\frac{\hbar^2}{2m}\right)[\nabla^2 + \nabla\cdot(V_\tau(\mathbf{r})\nabla)] + V_{\rm eff}(\mathbf{r}). \tag{11}$$

Here the effective potential has the electron-nuclear $[V_N(\mathbf{r})]$ and electron-electron (Hartree) $[V_H(\mathbf{r})]$ potential energy contributions in addition to the effective exchange-correlation term:

$$V_{\rm eff}(\mathbf{r}) = V_N(\mathbf{r}) + V_H(\mathbf{r}) + V_{xc}(\mathbf{r}). \tag{12}$$

From a knowledge of the self-consistent eigenstate energies ε_i of the generalized Kohn-Sham equations [Eq. (10)], another expression of the electronic total energy [Eq. (1)] can be written

$$E_{\rm tot} = \sum_i w_i\varepsilon_i - E_H + E_{xc} - \int d^3r[V_{xc}(\mathbf{r})n(\mathbf{r}) - V_\tau(\mathbf{r})\tau(\mathbf{r})]. \tag{13}$$

Here the subtracted terms are typically referenced as the "double-counting" corrections, and that last term of the expression is unique to the meta-GGA formulation.

3. Self-consistent generalized Kohn-Sham equations for an all-electron spherical atom

For a spherical or spherically averaged atom, the wave function can be written

$$\Phi_i(\mathbf{r}) = \frac{\varphi_{n_i l_i}(r)}{r} Y_{l_i m_i}(\hat{\mathbf{r}}), \tag{14}$$

where all spherical harmonic components $Y_{lm}(\hat{\mathbf{r}})$ are assumed to contribute equally. Correspondingly, the electron density can be calculated in terms of the radial wave functions $\varphi_{nl}(r)$ and their occupancies w_{nl} according to

$$n(r) = \frac{1}{4\pi r^2}\sum_{nl} w_{nl}|\varphi_{nl}(r)|^2. \tag{15}$$

The corresponding derivative expressions for the spherically symmetric system are given by

$$\nabla n = \frac{\partial n}{\partial r}\hat{\mathbf{r}} \quad \text{and} \quad \nabla^2 n = \frac{\partial^2 n}{\partial r^2} + \frac{2}{r}\frac{\partial n}{\partial r}, \tag{16}$$

$$V_{xc}(r) = \frac{\partial f_{xc}}{\partial n} - \frac{\partial}{\partial r}\left(2\frac{\partial f_{xc}}{\partial\sigma}\frac{\partial n}{\partial r}\right) - \frac{2}{r}\left(2\frac{\partial f_{xc}}{\partial\sigma}\frac{\partial n}{\partial r}\right) + \frac{\partial^2}{\partial r^2}\left(\frac{\partial f_{xc}}{\partial(\nabla^2 n)}\right) + \frac{2}{r}\frac{\partial}{\partial r}\left(\frac{\partial f_{xc}}{\partial(\nabla^2 n)}\right). \tag{17}$$

Similarly, $\tau(r)$ for the spherical atom can be calculated from the expression

$$\tau(r) = \frac{\hbar^2}{2m}\frac{1}{4\pi r^2}\sum_{nl} w_{nl}\tau_{nl}(r), \tag{18}$$

where

$$\tau_{nl}(r) \equiv \left(\frac{d\varphi_{nl}(r)}{dr} - \frac{\varphi_{nl}(r)}{r}\right)^2 + l(l+1)\left(\frac{\varphi_{nl}(r)}{r}\right)^2. \tag{19}$$

This last result was derived by Yao and Kanai in Ref. [17] from the properties of spherical harmonic functions.

The radial generalized Kohn-Sham equation for each orbital $\varphi_{nl}(r)$ of the spherical system can be written

$$H(r)\varphi_{nl}(r) = \varepsilon_{nl}\varphi_{nl}(r), \tag{20}$$

where

$$H(r) = -\frac{\hbar^2}{2m}K(r) + V_{\text{eff}}(r), \tag{21}$$

with the radial kinetic energy operator

$$K(r) \equiv (1 + V_\tau(r))\left(\frac{d^2}{dr^2} - \frac{l(l+1)}{r^2}\right) + \frac{dV_\tau(r)}{dr}\left(\frac{d}{dr} - \frac{1}{r}\right). \tag{22}$$

Finite-difference algorithms are generally useful for solving the radial (generalized) Kohn-Sham equations and can be used to solve Eq. (20). For a solution of the Kohn-Sham equations without the first derivative term, the Numerov algorithm [28] is highly efficient. However, in the present case it is convenient to transform to two coupled first-order equations such as given by the following form [29] in terms of the functions $y_1(r)$ and $y_2(r)$ and coupling functions $z_{ij}(r)$:

$$\begin{aligned}\frac{dy_1(r)}{dr} &= z_{11}(r)y_1(r) + z_{12}(r)y_2(r),\\ \frac{dy_2(r)}{dr} &= z_{21}(r)y_1(r) + z_{22}(r)y_2(r).\end{aligned} \tag{23}$$

These can be used with the following relationships:

$$\begin{aligned} y_1(r) &= \varphi_{nl}(r), \qquad y_2(r) = [1 + V_\tau(r)]\frac{d\varphi_{nl}(r)}{dr},\\ z_{11}(r) &= 0 = z_{22}(r), \quad z_{12}(r) = \frac{1}{[1 + V_\tau(r)]},\\ z_{21}(r) &= [1 + V_\tau(r)]\frac{l(l+1)}{r^2} + \frac{[dV_\tau(r)]}{dr}\frac{1}{r}\\ &\quad + \frac{2m}{\hbar^2}[V_{\text{eff}}(r) - \varepsilon_{nl}]. \end{aligned} \tag{24}$$

However, it is our experience that because of the high sensitivity of $V_\tau(r)$ and $V_{xc}(r)$ to the detailed values of the number $n(r)$ and kinetic energy $\tau(r)$ densities, these and other finite-difference algorithms are ineffective for finding the self-consistent atomic bound states. Consequently, we developed a spline solver scheme based on the cubic spline interpolation formalism developed by Ahlberg *et al.* [30] and by de Boor [31]. The main idea is to discretize the radial extent of atomic bound-state wave functions so that the differential form of the generalized Kohn-Sham equation can be combined with the cubic spline continuity conditions into an algebraic eigenvalue problem,

$$\mathbf{\Lambda} Q_{nl} = \varepsilon_{nl} Q_{nl}. \tag{25}$$

Here $\mathbf{\Lambda}$ is an $n_s \times n_s$ matrix and Q_{nl} is an eigenvector of length n_s related to the radial wave function. Denoting the discrete radial points by r_k, the indices $k = 1, 2, \ldots n_s$ are used in Eq. (25). The origin $r_0 \equiv 0$ is not included in the eigenvalue matrix evaluation by virtue of the fact that by design, $\varphi_{nl}(0) = 0$. Additionally, for bound states it is reasonable to assume that $\varphi_{nl}(r_{n_s+1}) = 0$. The details of the construction of Eq. (25) and its use in determining the bound-state Kohn-Sham one-electron energies ε_{nl} and corresponding bound-state radial wave functions $\varphi_{nl}(r)$ are presented in Appendix A. From these solutions, for all of the occupied bound states nl, the electron number $n(r)$ and kinetic energy $\tau(r)$ densities are calculated from Eqs. (15) and (18), respectively. A further algorithmic design adjustment made for treating the high sensitivity of $V_\tau(r)$ and $V_{xc}(r)$ was to iterate the electron density for achieving self-consistency rather than the usual procedure based on iterating the Kohn-Sham potential.

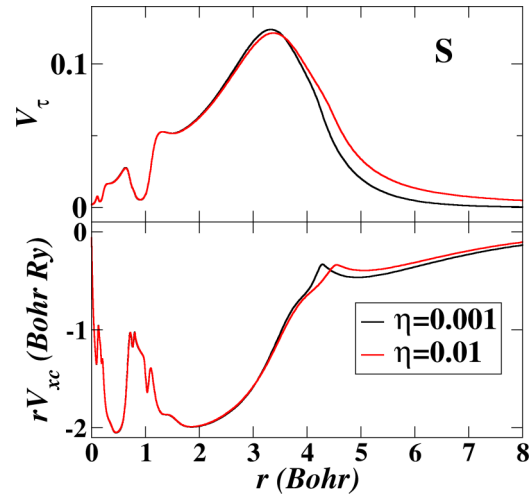

FIG. 1. Comparison of the self-consistent radial potentials $rV_{xc}(r)$ and $V_\tau(r)$ for S using the r2SCAN functional with $\eta = 0.01$ and $\eta = 0.001$.

B. Self-consistent results for spherical atoms having no net spin

We implemented these equations in the ATOMPAW code [19] for the rSCAN functional of Bartók and Yates [14] and for the r2SCAN functional of Furness *et al.* [15] using a slightly modified form for numerical stabilization (using parameter $\eta = 0.01$ in addition to its original value of $\eta = 0.001$). The parameter η specifically effects the dependence of the functional on the kinetic energy density through the intermediate function $\bar{\alpha}$, which is defined [15]

$$\bar{\alpha}(\mathbf{r}) \equiv \frac{\tau(\mathbf{r}) - \tau_W(\mathbf{r})}{\tau_{\text{unif}}(\mathbf{r}) + \eta\tau_W(\mathbf{r})}, \tag{26}$$

where

$$\tau_W \equiv \frac{|\nabla n|^2}{8n} \quad \text{and} \quad \tau_{\text{unif}} \equiv \frac{3n}{10}(3\pi^2 n)^{2/3}. \tag{27}$$

Reference [15] mentions possible choices of the "regularization parameter" η, and upon consulting with the authors, it is our understanding that the choice of $\eta = 0.01$ is within the range of the functional design. We find this choice to have numerical advantages over the choice of $\eta = 0.001$, as discussed for a few examples in the following. Of course, a more comprehensive study will be needed to understand its representability of exchange-correlation effects in the full range of materials simulations.

In order to assess the sensitivity of the r2SCAN functional to the η parameter, we compare $V_\tau(r)$ and $rV_{xc}(r)$ for the two values of η for two different atoms. Figure 1 shows the results for the atom S, in which case the difference is relatively small

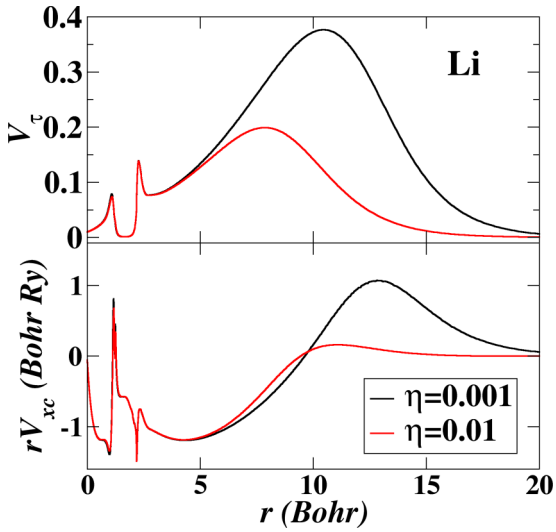

FIG. 2. Comparison of the self-consistent radial potentials $rV_{xc}(r)$ and $V_\tau(r)$ for Li using the r2SCAN functional with $\eta = 0.01$ and $\eta = 0.001$. For this case, $n_s = 2000$ was used.

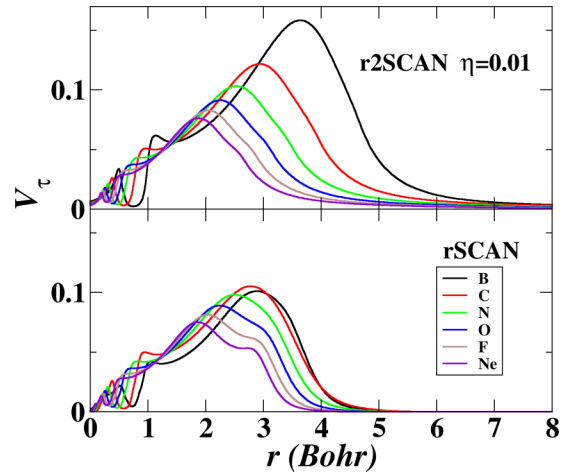

FIG. 3. $V_\tau(r)$ for elements in the second row of the periodic table.

and occurs for large distances from the atom. A different profile is seen for atoms in the first two columns of the periodic table, as shown in Fig. 2 for the Li atom. In this case, in order to avoid the rapid oscillations produced by our numerical algorithm in the evaluation of $V_\tau(r)$ and $V_{xc}(r)$ for $r > 10$ Bohr, particularly for $\eta = 0.001$, it is necessary to choose $n_s = 2000$, as explained in Appendix A. These oscillations do not affect the calculated energies for this case but do illustrate the numerical sensitivity of the r2SCAN functional with $\eta = 0.001$. Additionally, the large repulsive potential contributions to $rV_{xc}(r)$ and enlarged values of $V_\tau(r)$ for $r > 10$ Bohr are reduced for the $\eta = 0.01$ formulation. While we originally wrote an explicit r2SCAN code within ATOMPAW, recently both the original r2SCAN and the modified r2SCAN01 (using $\eta = 0.01$) versions are now available in the LIBXC library [24,25].

The results for the self-consistent radial dimensionless kinetic potential $V_\tau(r)$ and for the effective exchange-correlation potential $V_{xc}(r)$ for atoms in the second and third rows and columns 13–18 of the periodic table are shown in Figs. 3–6. For these columns of the periodic table, it is interesting to note the consistent radial patterns of the functions for these consecutive atoms. From these results and those of Figs. 1 and 2, we see that the radial dimensionless kinetic potentials are small with a typical range of $0 \leqslant V_\tau(r) \leqslant 0.5$.

Table I summarizes all the electron ground-state energies calculated for the rSCAN [14] and for the r2SCAN [15] functionals. The last column of the table lists the energy differences between the two choices of η, showing these differences to be on the order of 0.001 Ry/electron for the atoms considered so far, including a few transition metals.

While this limited study suggests that computed energies are rather insensitive to the choice of η, a more comprehensive study could perhaps determine an optimal choice of η for the most effective use of the r2SCAN functional for studying a large range of materials systems.

It is also interesting to see how the shape of the r2SCAN $V_{xc}(r)$ compares with other exchange-correlation functional forms, as is illustrated for Si in Fig. 7. Here the detailed structures of the r2SCAN functional compared with the other functionals are apparent.

III. PROJECTOR AUGMENTED-WAVE (PAW) FORMALISM

The PAW formalism of Blöchl [18] is based on constructing an all-electron and pseudo-Hamiltonian systems which differ from each other only within an augmentation sphere of radius r_c^a for each atom a. By construction, the pseudo-Hamiltonian system must be composed of spatially smooth contributions in order to benefit from numerically efficient computation. One advantage of the PAW method is that in principle the all-electron contributions to the system are well approximated (usually within the frozen-core approximation). In addition to the original formulation by Blöchl [18], many details of the method have appeared in the literature [19,34–41]. Here we focus on the aspects of the PAW method that

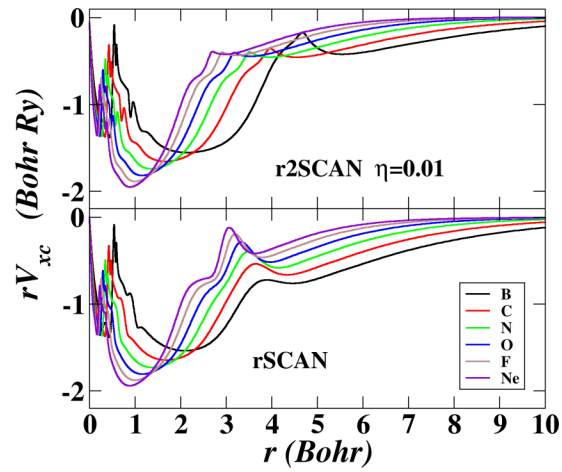

FIG. 4. $rV_{xc}(r)$ for elements in the second row of the periodic table.

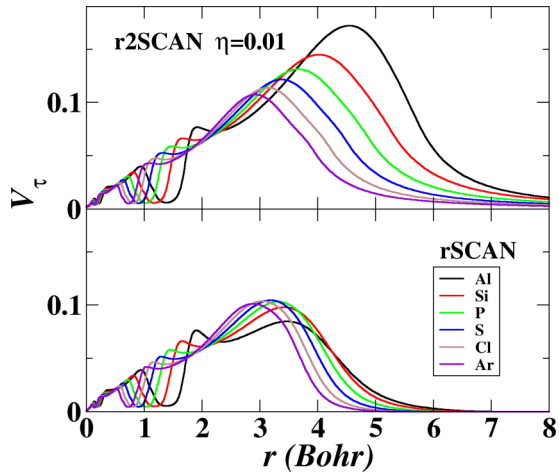

FIG. 5. $V_\tau(r)$ for elements in the third row of the periodic table.

are effected by the introduction of the generalized Kohn-Sham equations and the dimensionless kinetic potential.

A. Treatment of core electrons

While it is possible to extend the PAW formalism beyond the frozen-core approximation [18,42], the present work is designed within that framework, which has been well documented [43]. For each atom a we divide the electronic density into (frozen) core $[n^a_{\rm core}(r)]$ and (variational) valence densities $[n^a(r)]$:

$$n(r) \to n^a_{\rm core}(r) + n^a(r). \tag{28}$$

The kinetic energy density function can be partitioned in a similar way:

$$\tau(r) \to \tau^a_{\rm core}(r) + \tau^a(r). \tag{29}$$

In general, the core contributions are confined to a small sphere near the atomic nucleus; however, their effects are numerically important in the evaluation of the exchange-correlation contributions in regions of significant core-valence overlap because of the highly nonlinear form of the functionals, as pointed out by Louie *et al.* [44].

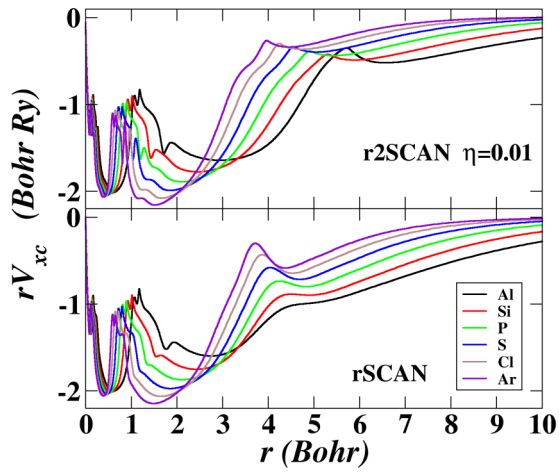

FIG. 6. $rV_{xc}(r)$ for elements in the third row of the periodic table.

Pseudofunctions will be indicated with a tilde symbol to distinguish them from their all-electron analogs. For example, it is convenient to construct pseudo core densities $\tilde{n}^a_{\rm core}(r)$ and pseudo core kinetic energy densities $\tilde{\tau}^a_{\rm core}(r)$ from their all-electron analogs $n^a_{\rm core}(r)$ and $\tau^a_{\rm core}(r)$. The pseudofunctions related to core electrons must be explicitly designed to meet numerical smoothness properties while preserving their physical effects on the valence electrons for $r \geqslant r^a_c$. For the pseudo core density function, the ATOMPAW code constructs $\tilde{n}^a_{\rm core}(r)$ to represent the tail of the core density for $r > r^a_c$ and a smooth continuous function for $r < r^a_c$, analogous to the nonlinear core correction of Louie *et al.* [44]. In particular, we choose

$$4\pi r^2 \tilde{n}^a_{\rm core}(r) \equiv \begin{cases} r^P \sum_{m=0}^{M} (U_m r^{2m}) & \text{for} \quad r \leqslant r^a_c \\ 4\pi r^2 n^a_{\rm core}(r) & \text{for} \quad r \geqslant r^a_c, \end{cases} \tag{30}$$

where the constants U_m are chosen so that $\tilde{n}^a_{\rm core}(r) \equiv n^a_{\rm core}(r)$ at $M+1$ consecutive points in the neighborhood of r^a_c. In practice, $P = 2$ and $M = 4$ are used. For the pseudo core kinetic energy density, we must also construct $\tilde{\tau}^a_{\rm core}(r)$ with a similar approach using

$$4\pi r^2 \tilde{\tau}^a_{\rm core}(r) \equiv \begin{cases} r^P \sum_{m=0}^{M} (W_m r^{2m}) & \text{for} \quad r \leqslant r^a_c \\ 4\pi r^2 \tau^a_{\rm core}(r) & \text{for} \quad r \geqslant r^a_c, \end{cases} \tag{31}$$

where the constants W_m are chosen so that $\tilde{\tau}^a_{\rm core}(r) \equiv \tau^a_{\rm core}(r)$ at $M+1$ consecutive points in the neighborhood of r^a_c. In practice, $P = 4$ and $M = 4$ are used. This choice ensures that both $\tilde{n}^a_{\rm core}(r)$ and $\tilde{\tau}^a_{\rm core}(r)$ are both smooth and have continuous derivatives. An example is illustrated in Fig. 8 for the case of Si, where we have chosen $r^a_c = 1.7$ Bohr with the core configuration of $1s^2 2s^2 2p^6$.

B. Treatment of valence electrons

The focus of the PAW calculation is the self-consistent treatment of the valence electrons. By virtue of the PAW formulation, the pseudo valence electron density and kinetic energy density also differ from their all-electron analogs $n^a(r)$ and $\tau^a(r)$ only within the augmentation sphere of radius r^a_c:

$$\tilde{n}^a(r) = n^a(r) \;\text{ for } r > r^a_c \quad \text{and} \quad \tilde{\tau}^a(r) = \tau^a(r) \;\text{ for } r > r^a_c. \tag{32}$$

The details of the behavior of $\tilde{n}^a(r)$ and of $\tilde{\tau}^a(r)$ for $0 \leqslant r \leqslant r^a_c$ depend on the chosen PAW construction scheme as discussed below.

The pseudo Hamiltonian analogous to Eq. (11) can be assumed to take the form

$$\tilde{H}(\mathbf{r}) = -\frac{\hbar^2}{2m}[\nabla^2 + \nabla \cdot (\tilde{V}_\tau(\mathbf{r})\nabla)] + \tilde{V}_{\rm eff}(\mathbf{r}), \tag{33}$$

where $\tilde{V}_{\rm eff}(\mathbf{r})$ denotes the self-consistent pseudopotential. Here it is assumed that

$$\tilde{H}(\mathbf{r}) = H(\mathbf{r}) \quad \text{for} \quad r \geqslant r^a_c. \tag{34}$$

The pseudopotential $\tilde{V}_{\rm eff}(\mathbf{r})$ must be constructed consistent with the continuity condition

$$\tilde{V}_{\rm eff}(\mathbf{r}) \equiv V_{\rm eff}(\mathbf{r}) \quad \text{for} \quad r \geqslant r^a_c. \tag{35}$$

The dimensionless pseudo kinetic potential $\tilde{V}_\tau(\mathbf{r})$ must also satisfy the continuity condition

$$\tilde{V}_\tau(r) \equiv V_\tau(r) \;\text{ for } r \geqslant r^a_c, \tag{36}$$

TABLE I. Total energy results (in Ry) calculated for the rSCAN ([14]) and r2SCAN ([15]) functionals for various atoms, comparing rSCAN and r2SCAN using $\eta = 0.01$ and $\eta = 0.001$. The column "Δr2SCAN" lists the difference in the two r2SCAN formulations.

Atom	rSCAN	r2SCAN ($\eta = 0.01$)	r2SCAN ($\eta = 0.001$)	Δr2SCAN
H	–0.906	–0.906	–0.906	0.000
He	–5.810	–5.810	–5.810	0.000
Li	–14.933	–14.932	–14.931	–0.001
Be	–29.302	–29.299	–29.298	0.001
B	–49.231	–49.218	–49.216	–0.002
C	–75.533	–75.512	–75.508	–0.004
N	–108.885	–108.855	–108.850	–0.005
O	–149.961	–149.920	–149.914	–0.006
F	–199.426	–199.373	–199.366	–0.008
Ne	–257.945	–257.879	–257.870	–0.009
Na	–324.572	–324.494	–324.484	–0.010
Mg	–400.192	–400.100	–400.089	–0.012
Al	–484.765	–484.653	–484.639	–0.014
Si	–578.754	–578.625	–578.610	–0.015
P	–682.480	–682.335	–682.318	–0.017
S	–796.263	–796.100	–796.082	–0.019
Cl	–920.417	–920.236	–920.216	–0.020
Ar	–1055.257	–1055.057	–1055.035	–0.022
Sc	–1521.390	–1521.126	–1521.099	–0.027
Cu	–3281.547	–3281.043	–3280.998	–0.044

which can be accomplished by using the core and valence number and kinetic energy pseudodensities in the exchange-correlation integrand Eq. (6). Explicitly, the dimensionless pseudo kinetic potential is determined by taking the functional derivative of that integrand with respect to the valence pseudo kinetic energy density, which, using an obvious notational simplification, can be written

$$\tilde{V}_\tau(r) = \frac{\partial f_{xc}\left[\tilde{n}^a_{\rm core}(r) + \tilde{n}^a(r), \tilde{\tau}^a_{\rm core}(r) + \tilde{\tau}^a(r)\right]}{\partial \tilde{\tau}^a(r)}. \quad (37)$$

Due to the presence of the $\tilde{V}_\tau(\mathbf{r})$ term, $\tilde{H}(\mathbf{r})$ differs from pseudo Hamiltonians constructed for exchange-correlation functionals that do not have kinetic energy density dependence. Schemes previously developed for constructing the basis functions $\{\tilde{\varphi}_{n_i l_i}(r)\}$ and projector functions $\{\tilde{p}_{n_i l_i}(r)\}$ must be adjusted accordingly. [Note that the notation $\tilde{p}_{n_i l_i}(r)$ is used as in Eq. (14) to relate the radial projector function to the three-dimensional projector function $P_i(\mathbf{r})$ with the appropriate spherical harmonic function.] For example, the following sequence of steps can be developed for PAW atomic datasets in the presence of kinetic energy density–dependent exchange-correlation functionals.

1. Perform a self-consistent generalized density-functional-theory calculation for the spherical atom in a given reference configuration (usually the ground state).

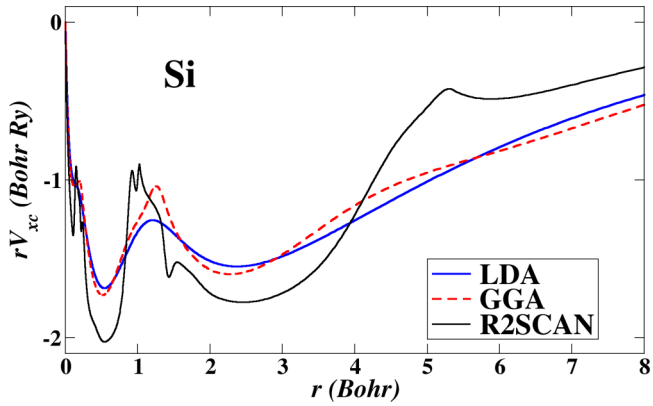

FIG. 7. Comparison of the self-consistent radial potentials $rV_{xc}(r)$ for Si for the LDA [32], GGA [33], and r2SCAN ($\eta = 0.01$) functionals.

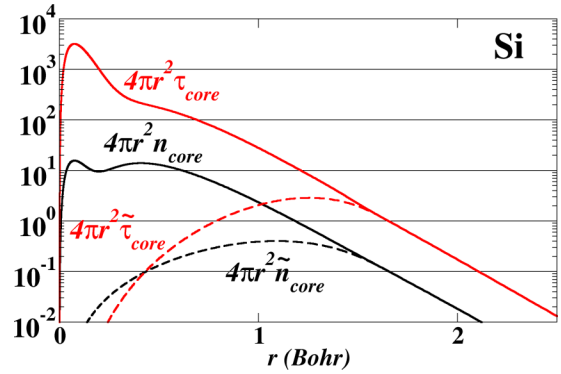

FIG. 8. For a Si atom, plot of the core density $4\pi r^2 n_{\rm core}(r)$ (black full line) and the core pseudodensity $4\pi r^2 \tilde{n}_{\rm core}(r)$ (black dashed line) in units of (1/Bohr). Also plotted is the core kinetic energy density $4\pi r^2 \tau_{\rm core}(r)$ (red full line) and the core pseudo kinetic energy density $4\pi r^2 \tilde{\tau}_{\rm core}(r)$ (red dashed line) in units of (Ry/Bohr). The core configuration is $1s^2 2s^2 2p^6$.

Form the core number and kinetic energy densities $n^a_{\rm core}(r)$ and $\tau^a_{\rm core}(r)$ and their pseudocounterparts $\tilde{n}^a_{\rm core}(r)$ and $\tilde{\tau}^a_{\rm core}(r)$.

2. Choose the all-electron atomic basis set $\{\varphi^a_{n_i l_i}(r)\}$ to represent the electronic valence states in nonspherical and excited configurations within materials of interest. This set should include all of the valence electron states found in step **#1** as well as exited and continuum-state solutions of Eq. (20). (Note that the notation with counting index i is used to imply both bound and continuum basis functions.)

3. For each all-electron basis function $n_i l_i$, construct the corresponding pseudo basis function $\tilde{\varphi}^a_{n_i l_i}(r)$ satisfying the condition

$$\tilde{\varphi}^a_{n_i l_i}(r) \equiv \varphi^a_{n_i l_i}(r) \quad \text{for} \quad r \geqslant r^a_c, \tag{38}$$

ensuring a smooth functional transition in the neighborhood of r^a_c. Note that in practice, knowledge of the all-electron and pseudo basis functions is only needed within the augmentation radius so that the long-range behavior of continuum functions poses no problems. As mentioned in the introduction of Sec. III, there are many schemes described in the literature to construct pseudo basis functions without the norm conservation condition as pioneered in the ultrasoft pseudopotential formalism [45].

4. Construct the valence pseudo kinetic energy density function $\tilde{\tau}^a(r)$. This is accomplished smoothly by using the core pseudo kinetic energy density $\tilde{\tau}^a_{\rm core}(r)$ found in step #1 and using the occupied pseudo basis functions $\tilde{\varphi}^a_{n_i l_i}(r)$ to construct the valence pseudo kinetic energy density $\tilde{\tau}^a(r)$. From the knowledge of the core and valence pseudo densities and pseudo kinetic energy densities, the corresponding functional derivative can be evaluated using Eq. (37) to determine the dimensionless pseudo kinetic potential $\tilde{V}_\tau(r)$.

5. Construct the screened pseudopotential $\tilde{V}_{\rm eff}(\mathbf{r})$. Note that some of the construction schemes need to know $\tilde{V}_\tau(r)$ from step #4.

6. For each pseudo basis function $\tilde{\varphi}^a_{n_i l_i}(r)$ determine the projector function $\tilde{p}^a_{n_i l_i}(r)$ which are confined to the augmentation sphere:

$$\tilde{p}^a_{n_i l_i}(r) \equiv 0 \quad \text{for} \quad r > r^a_c. \tag{39}$$

The corresponding full three-dimensional functions satisfy the condition

$$\left\langle \tilde{P}^a_{n_i l_i m_i} \middle| \tilde{\Phi}^a_{n_j l_j m_j} \right\rangle = \delta_{n_i n_j} \delta_{l_i l_j} \delta_{m_i m_j}. \tag{40}$$

7. Unscreen the screened pseudopotential $\tilde{V}_{\rm eff}(\mathbf{r})$ in order to find the local pseudopotential needed to perform self-consistent pseudopotential calculations for condensed matter systems.

Details of some of these steps are presented below.

Construction of pseudo basis functions $\{\tilde{\varphi}^a_{n_i l_i}(r)\}$ (# 3)

The pseudo basis functions $\tilde{\varphi}_{n_i l_i}(r)$ are conveniently constructed from an assumed smooth functional form for $r \leqslant r^a_c$ which smoothly matches the all-electron eigenfunction at $r = r^a_c$, $\varphi_{n_i l_i}(r)$ evaluated at the energy $\varepsilon_{n_i l_i}$:

$$\tilde{\varphi}_{n_i l_i}(r) = \begin{cases} g_{l_i}(r) & \text{for} \quad r \leqslant r^a_c \\ \varphi_{n_i l_i}(r) & \text{for} \quad r > r^a_c \end{cases}. \tag{41}$$

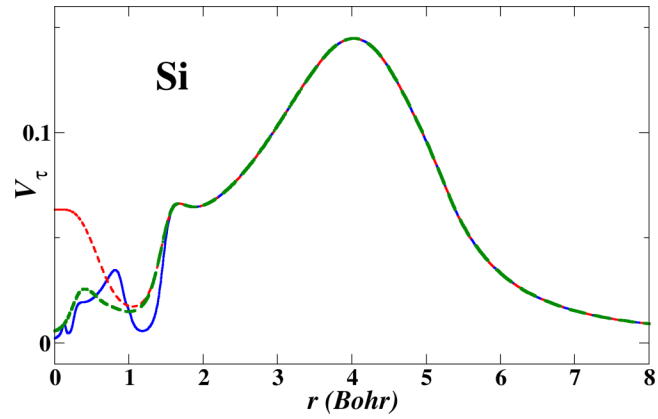

FIG. 9. Plot of $V_\tau(r)$ (full blue line) and $\tilde{V}_\tau(r)$ (dashed red line) evaluated using Eq. (37) for Si for the r2SCAN $\eta = 0.01$ case. The analogous form of Kresse [Eq. (43)], $\tilde{V}^K_\tau(r)$, is indicated with the green dashed line.

Here $g_{l_i}(r)$ is typically chosen as a sum of polynomial or Bessel functions and has the characteristic form near the origin of

$$g_{l_i}(r) \underset{r\to 0}{\propto} r^{l_i+1}. \tag{42}$$

Coefficients within the smooth functions $g_{l_i}(r)$ are most easily evaluated by matching with $\varphi_{n_i l_i}(r)$ at a sequence of consecutive points $r \leqslant r^a_c$.

Construction of the dimensionless pseudo kinetic potential $\tilde{V}_\tau(r)$ (# 4)

From a knowledge of the pseudo basis functions which correspond to occupied valence states, the valence pseudodensity $\tilde{n}^a(r)$ and valence pseudo kinetic energy density $\tilde{\tau}^a(r)$ can be determined and the corresponding dimensionless pseudo kinetic potential $\tilde{V}_\tau(r)$ can be evaluated using Eq. (37). Figure 9 illustrates the example of Si using the r2SCAN $\eta = 0.01$ case. For completeness, we also include the alternative formulation introduced by Kresse and Joubert [35], which includes the valence compensation charge $\hat{n}^a(r)$ (defined below in the context of the electrostatic energy) into the exchange-correlation integrand, resulting in a somewhat different dimensionless pseudo kinetic potential:

$$\tilde{V}^K_\tau(r) = \frac{\partial f_{xc}\left[\tilde{n}^a_{\rm core}(r) + \tilde{n}^a(r) + \hat{n}^a(r), \tilde{\tau}^a_{\rm core}(r) + \tilde{\tau}^a(r)\right]}{\partial \tilde{\tau}^a(r)}. \tag{43}$$

While, by design, $\hat{n}^a(r)$ vanishes for $r \geqslant r^a_c$, its presence in Eq. (43) should do no harm. However, in previous work [41] we have noted that the inclusion of compensation charge density in the exchange-correlation evaluation can cause difficulties in some cases. More generally, we note that because the subsequent steps of pseudopotential construction depend on the dimensionless pseudo kinetic potential, the Kresse formulation will generate different screened and unscreened pseudopotential functions and different projector functions. By contrast, LDA or GGA pseudopotential formulations differ between the Blöchl and Kresse formulations only in the unscreened pseudopotential form. In the following, most of

the results are generated with the Blöchl formulation using $\tilde{V}_\tau(r)$ defined in Eq. (37) unless otherwise indicated.

Construction of the screened pseudopotential $\tilde{V}_{\rm eff}(\mathbf{r})$ (# 5)

There are many schemes in the literature describing the construction of $\tilde{V}_{\rm eff}(\mathbf{r})$, all satisfying the continuity condition Eq. (35). There is often an accuracy advantage in using schemes derived from inverting the Kohn-Sham equations for a particular wave function $\tilde{\varphi}_l^{\rm PS}(r)$ based on its corresponding all-electron function $\varphi_l^{\rm AE}(r)$ at energy $\varepsilon_l^{\rm AE}$ as was developed for norm-conserving pseudopotentials [46–48]. Here the index l represents a particular angular momentum channel, and the construction state, characterized by energy $\varepsilon_l^{\rm AE}$, typically represents an excited (positive energy) state of the system not spanned by the set of all-electron and pseudo basis functions $\{\varphi_{n_i l_i}(r)\}$ and $\{\tilde{\varphi}_{n_i l_i}(r)\}$. For example, following the scheme of Kerker [47], it is convenient to construct this pseudo wave function as

$$\tilde{\varphi}_l^{\rm PS}(r) = \begin{cases} r^{l+1} e^{f(r)} & \text{for } r \leqslant r_c^a \\ \varphi_l^{\rm AE}(r) & \text{for } r > r_c^a. \end{cases} \tag{44}$$

Given this wave-function form, $\tilde{V}_{\rm eff}(\mathbf{r})$ is determined as the potential which satisfies the spherically symmetric form of the generalized Kohn-Sham equation, Eq. (33). Typically, the function $f(r)$ is a polynomial whose coefficients are determined from the continuity and smoothness conditions of $\tilde{\varphi}_l^{\rm PS}(r) = \varphi_l^{\rm AE}(r)$ for $r > r_c^a$ and (optionally) norm-conservation conditions for $0 \leqslant r \leqslant r_c^a$. In terms of $f(r)$, the potential within the augmentation sphere ($r \leqslant r_c^a$) can be written as

$$\tilde{V}_{\rm eff}(r) = \varepsilon_l^{\rm AE} + \frac{\hbar^2}{2m} X(r), \tag{45}$$

where

$$X(r) \equiv (1+\tilde{V}_\tau)\left(\frac{d^2 f}{dr^2} + \left(\frac{df}{dr}\right)^2 + \frac{2(l+1)}{r}\frac{df}{dr}\right) + \frac{d\tilde{V}_\tau}{dr}\left(\frac{df}{dr} + \frac{l}{r}\right). \tag{46}$$

This expression can be evaluated, since the dimensionless kinetic potential $\tilde{V}_\tau$ would have been determined in step #4. Also note that $\tilde{V}_\tau$ controls features of the functional form of the pseudopotential. For example, for $r \to 0$ and $l > 0$ the function diverges unless $\frac{d\tilde{V}_\tau}{dr}\big]_{r\to 0} = 0$. We note that for the example of Si shown in Fig. 9, $\tilde{V}_\tau(r)$ does have zero slope at the origin. More generally, we note that not all of the features of pseudopotential construction documented in the literature can be realized for the MGGA case due to the presence of the predetermined function $\tilde{V}_\tau(r)$. For example, the zero-curvature condition at $r = 0$ implemented in the Troullier and Martins [48] scheme is more complicated in this case and has not been implemented in ATOMPAW.

Construction of projector functions (# 6)

There are also many schemes in the literature [18,34,35,45] for constructing the PAW projector functions, many of which are implemented in ATOMPAW and some of which are altered by the generalized Kohn-Sham equations due to the kinetic energy density contributions of V_τ and $\tilde{V}_\tau$. For example, if a Vanderbilt-like method [45] is used, the radial projector functions $\{\tilde{p}_{n_i l_i}(r)\}$ are derived from a knowledge of the pseudo radial basis functions $\tilde{\varphi}_{n_i l_i}(r)$ and their all-electron energies $\varepsilon_{n_i l_i}$ as follows. Compute a localized auxiliary function

$$\chi_{n_i l_i}(r) = (\varepsilon_{n_i l_i} - \tilde{H}(r))\tilde{\varphi}_{n_i l_i}(r). \tag{47}$$

Here, analogous to Eqs. (21) and (22) the pseudo Hamiltonian [Eq. (33)] takes the form in radial coordinates,

$$\tilde{H}(r) = -\frac{\hbar^2}{2m}\tilde{K}(r) + \tilde{V}_{\rm eff}(r), \tag{48}$$

with the pseudo radial kinetic energy operator

$$\tilde{K}(r) \equiv [1+\tilde{V}_\tau(r)]\left(\frac{d^2}{dr^2} - \frac{l(l+1)}{r^2}\right) + \frac{d\tilde{V}_\tau(r)}{dr}\left(\frac{d}{dr} - \frac{1}{r}\right). \tag{49}$$

Once the auxiliary function is formed, the projectors can be determined in the usual way by constructing the linear combination

$$\tilde{p}_{n_i l_i}(r) = \sum_{n_j} \chi_{n_j l_i}(r)\left(\mathbf{B}^{-1}\right)_{n_j n_i}, \tag{50}$$

where the elements of matrix $\mathbf{B}$ are given by

$$\mathbf{B}_{n_i n_j} \equiv \int_0^{r_c} dr\, \tilde{\varphi}_{n_i l_i}(r)\chi_{n_j l_i}(r). \tag{51}$$

Note that this construction ensures that the projector functions are confined within the augmentation region and that they satisfy a generalized orthogonality condition of the form

$$\langle \tilde{p}_{n_i l_i} | \tilde{\varphi}_{n_j l_i} \rangle = \delta_{ij}. \tag{52}$$

Determination of the local pseudopotential by unscreening $\tilde{V}_{\rm eff}(\mathbf{r})$ (# 7)

The screened pseudopotential function $\tilde{V}_{\rm eff}(\mathbf{r})$ represents a neutral atom based on a particular electronic configuration. In order to use this potential in a solid containing this atom, it is imagined that the valence electrons will be reconfigured, leaving the core electrons and a residual potential. Because the PAW transformation does not conserve charge, similar to the case of ultrasoft pseudopotentials [45], Blöchl [18] introduced the notion of a compensation charge which is added and subtracted from the calculation to make sure that Coulombic interactions are accurately evaluated. The compensation charge is localized within the augmentation sphere and can take various shapes according to the optimal numerical performance. The valence compensation charge is denoted $\hat{n}^a(r)$. Typically, a unit of compensation charge is denoted by the normalized shape function $\hat{s}(r)$ and its associated electrostatic potential is denoted by $\hat{v}(r)$, such that

$$\nabla^2 \hat{v}(r) = -4\pi \hat{s}(r). \tag{53}$$

The valence compensation charge for atom a is then given by

$$\hat{n}^a(r) = \Delta Q^a \hat{s}(r), \tag{54}$$

where ΔQ^a plus the integral over the pseudo valence density represents the number of valence electrons in the atom. For an atom with atomic number Z^a and $Q^a_{\rm core}$ electrons,

$$\Delta Q^a \equiv Z^a - Q^a_{\rm core} - \int d^3 r \tilde{n}^a(r). \tag{55}$$

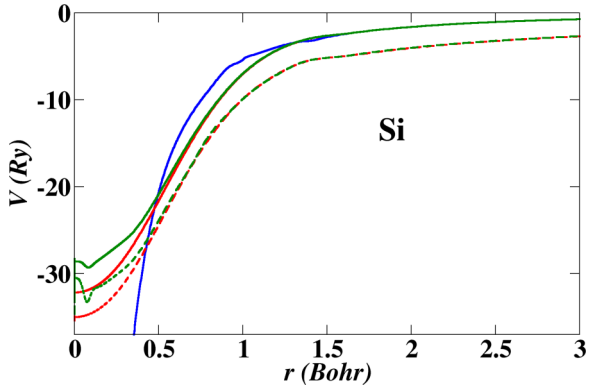

FIG. 10. Effective potentials for Si for the r2SCAN ($\eta = 0.01$) functional, comparing the self-consistent all-electron potential $V_{\rm eff}(r)$ (full blue line) with the screened pseudopotentials $\tilde{V}_{\rm eff}(r)$ (Blöchl scheme: full red line) and $\tilde{V}^K_{\rm eff}(r)$ (Kresse scheme: full green line). Also plotted are the corresponding unscreened pseudopotentials $V^a_{Z_c}(r)$ (Blöchl scheme: dashed red line) and $V^{aK}_{Z_c}(r)$ (Kresse scheme: dashed green line). The pseudopotentials were constructed using Eq. (45) where $l = 2$, $r^a_c = 1.7$ Bohr, and $f(r)$ is a six-term even polynomial with norm conservation imposed.

In practice, the pseudopotential unscreening formulation depends on the code for which the PAW dataset will be used. Here we use the formulation for the ABINIT code [20], which is similar but not identical to that of Kresse *et al.* [35] but differs from the original formulation of Blöchl [18] and from the formulation in early versions of ATOMPAW [19]. For each atom, we expect the self-consistent effective pseudopotential to take the form

$$\tilde{V}_{\rm eff}(r) = \tilde{V}^a_{Z_c}(r) + \tilde{V}_H(r) + \tilde{V}_{xc}(r). \tag{56}$$

The local ionic pseudopotential term $\tilde{V}^a_{Z_c}(r)$ replaces the electron-nucleus interaction in the all-electron formulation. The Hartree term is calculated from the self-consistent pseudo valence density and compensation charge:

$$\tilde{V}_H(r) = e^2 \int d^3r' \frac{\tilde{n}^a(r')}{|\mathbf{r} - \mathbf{r}'|} + e^2 \Delta Q^a \hat{v}(r). \tag{57}$$

The exchange term is expressed using the formulation in Eq. (17) with pseudodensity arguments:

$$\tilde{V}_{xc}(r) = V_{xc}\big(\tilde{n}^a_{\rm core} + \tilde{n}^a, \tilde{\tau}^a_{\rm core} + \tilde{\tau}^a\big). \tag{58}$$

In order to find $\tilde{V}^a_{Z_c}(r)$, we use the constructed valence pseudodensity $\tilde{n}^a(r)$ to unscreen $\tilde{V}_{\rm eff}(r)$:

$$\tilde{V}^a_{Z_c}(r) = \tilde{V}_{\rm eff}(r) - \tilde{V}_H(r) - \tilde{V}_{xc}(r). \tag{59}$$

Note that in this ABINIT formulation of the local potential, $\tilde{V}^a_{Z_c}(r)$ represents, at long range, the attractive potential due to the nuclear charge minus the core shell electrons (that is, the true valence charge):

$$\tilde{V}^a_{Z_c}(r) \underset{r\to\infty}{=} -e^2 \frac{Z^a - Q^a_{\rm core}}{r}. \tag{60}$$

An example of $\tilde{V}^a_{Z_c}(r)$ for Si is shown in Fig. 10, where the r2SCAN ($\eta = 0.01$) result is plotted with the corresponding screened pseudopotential $\tilde{V}_{\rm eff}(r)$ and all-electron potential $V_{\rm eff}(r)$. Also shown on that plot are the screened $\tilde{V}^K_{\rm eff}(r)$ and unscreened $\tilde{V}^{aK}_{Z_c}(r)$ pseudopotentials based on the Kresse formulation [35]. In this case the construction scheme introduced additional structure in the pseudopotentials which could perhaps be eliminated by adjusting the pseudopotential construction scheme.

The local ionic potential $\tilde{V}^a_{Z_c}(r)$ together with the basis and projector functions and the core densities $n^a_{\rm core}(r)$, $\tilde{n}^a_{\rm core}(r)$ and core kinetic energy densities $\tau^a_{\rm core}(r)$, $\tilde{\tau}^a_{\rm core}(r)$ are among the quantities that go into each atomic PAW dataset.

C. Assessment of PAW datasets

The best way to assess the PAW datasets is to use them in a variety of solid calculations, as will be discussed in Sec. IV. However, some results from ATOMPAW are also useful. The logarithmic derivatives of the radial wave functions evaluated at the augmentation radius r^a_c indicates the scattering properties of the effective potential for each angular momentum channel l. The comparison of the all-electron and pseudo logarithmic derivatives as a function of energy has been long used [46] as a measure of pseudopotential efficacy. The so-called phase-unwrapped arctangent of the logarithmic derivative defined by Brock *et al.* [49] is a convenient representation of the all-electron $[A_l(\varepsilon)]$ and pseudo $[\tilde{A}_l(\varepsilon)]$ logarithmic derivative using a continuous function. Rapid deviations of the curves by values of π may indicate unphysical ghost states [50]. For the all-electron values, Eq. (24) can be used to determine the all-electron radial function $\psi_{\varepsilon l}(r)$ in the range $0 \leqslant r \leqslant r^a_c + \delta$ (where δ denotes a small positive radial increment) at various energies ε. The details of the corresponding determination for the PAW radial function are given in Appendix B. An example of the resulting phase-unwrapped arctangents are presented in Fig. 11 for Cu. In this case, the curves for $A_l(\varepsilon)$ and $\tilde{A}_l(\varepsilon)$ are very close for the full energy range.

IV. ABINIT RESULTS

The software package ABINIT, versions $\geqslant$ 9.6.2, has implemented evaluation of meta-GGA terms, both in the plane-wave and localized terms [22]. Some details of the implementation are described in the Ph.D. thesis of Charraud [51]. Using LIBXC, it can perform meta-GGA evaluations from atomic datasets generated with the same functional or, by using the appropriate *ixc* keyword, from atomic datasets generated with a different functional. Using version 4.2.0.0 of ATOMPAW, we have constructed some self-consistent PAW datasets using similar parameter choices for testing. The input files for generating some of the atomic datasets used in this work are available in the Supplemental Materials [23]. Total electronic energies E as a function of lattice parameter a were calculated for three face-centered cubic materials using the exchange-correlation functionals Perdew-Burke-Ernzerhof (PBE) [33], PBESOL [52], r2SCAN [15], and r2SCAN01 using datasets constructed with the same functional. Additionally, using PBE datasets, we also used ABINIT to construct binding-energy curves with meta-GGA functionals using the notation `PBE + SCAN` for example. For the materials, the equilibrium cubic lattice parameter a_0, bulk modulus B_0, and pressure derivative of the bulk modulus B'_0 were all fit to the Birch-Murnaghan equation of state [53],

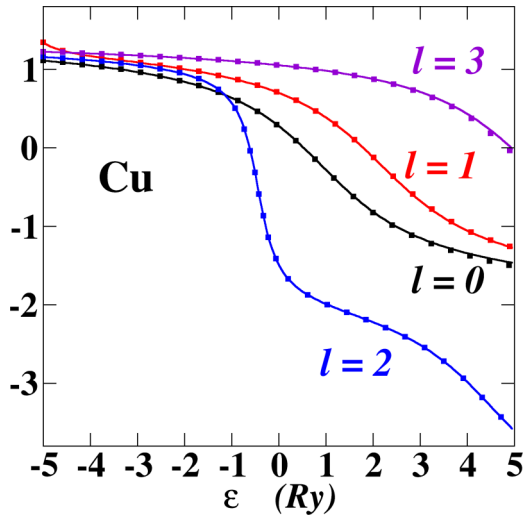

FIG. 11. Plot of of all-electron $A_l(\varepsilon)$ (full lines) and pseudo $\tilde{A}_l(\varepsilon)$ (enlarged dots) plotted in units of radians along the vertical axis for a Cu atom calculated using r2SCAN with $\eta = 0.01$ for the angular momentum channels $l = 0, 1, 2$, and 3 for the indicated energy range. In this case, the core states were taken to be $1s^2 2s^2 2p^6$, the valence configuration was $3s^2 3p^6 3d^{10} 4s^1 4p^0$, and the augmentation radius was $r_c^a = 1.8$ Bohr. The basis set included two basis functions for each l channel for $l = 0, 1, 2$, including a continuum state for $l = 2$.

which for the fcc lattice takes the form as a function of cubic lattice parameter a and the equation-of-state parameters E_0, a_0, B_0, B_0':

$$E(a; E_0, a_0, B_0, B_0') = E_0 + \frac{9a_0^3 B_0}{64}\left\{\left[\left(\frac{a_0}{a}\right)^2 - 1\right]^3 B_0' + \left[\left(\frac{a_0}{a}\right)^2 - 1\right]^2\left[6 - 4\left(\frac{a_0}{a}\right)^2\right]\right\}. \quad (61)$$

The results are listed in Table II, and the binding-energy plots are presented in Fig. 12.

From these limited results, some preliminary conclusions emerge. For example, the equation-of-state parameters for the r2SCAN and r2SCAN01 functionals are essentially identical and closer to experiment than results for the PBESOL and PBE functionals. Similar calculations for Si were reported by Yao and Kanai [17]. Their results for `PBE + SCAN` are somewhat differ from those reported in Table II but perhaps within the numerical uncertainty of the calculations. (We are not able to generate a self-consistent SCAN dataset to compare.) It is also interesting to note that the results for `PBE + r2SCAN` are quite close to the results for the self-consistent r2SCAN results for Si. The binding-energy curves for NaCl cover a much smaller energy range. On this scale, differences between the various binding-energy curves are more apparent. In this case we see significant differences between the r2SCAN binding-energy curves computed with the r2SCAN ("r2SCAN") and PBE ("`PBE + r2SCAN`") datasets.

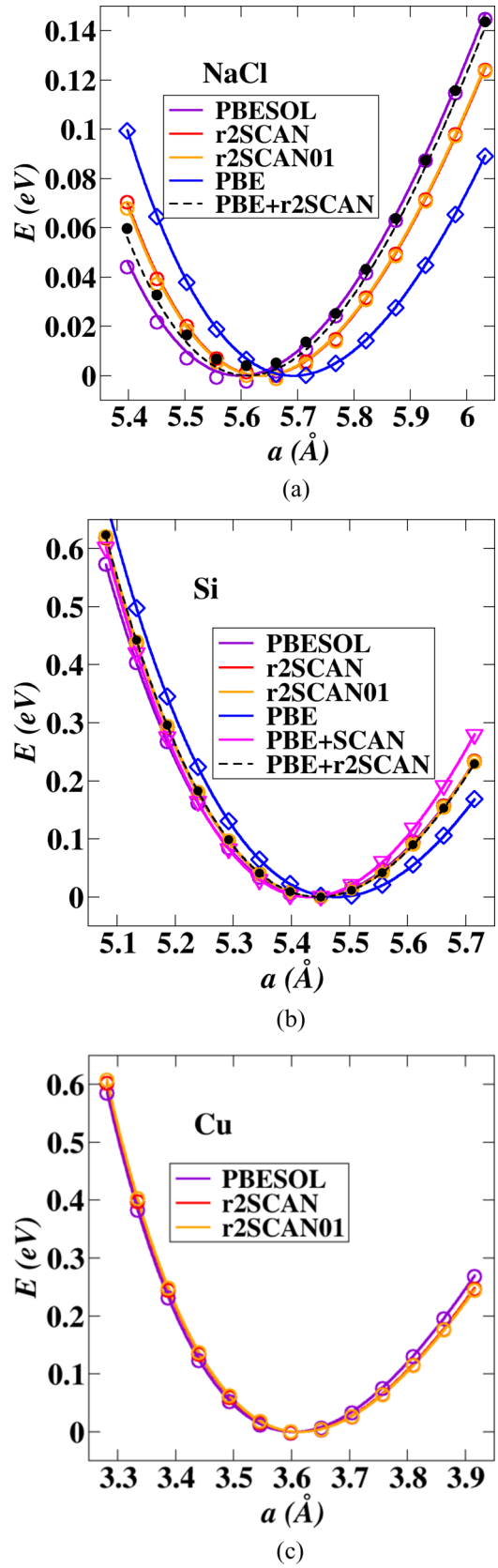

FIG. 12. Binding-energy plots for three face-centered cubic materials: (a) NaCl, (b) Si, and (c) Cu. Full lines represent fits to the Birch-Murnaghan equation of state Eq. (61), while symbols with the same color represent total energy results obtained from ABINIT.

TABLE II. Equation-of-state parameters determined from binding-energy curves generated from ABINIT calculations of various face-centered-cubic materials fit to the Birch-Murnaghan equation of state Eq. (61) including a_0 (in angstroms), B_0 (in 10^9 Pascals), and B_0'. Experimental results are quoted from Ref. [54].

System	a_0	B_0	B_0'
Si (PBESOL)	5.44	94	4.2
Si (r2SCAN01)	5.45	97	4.1
Si (r2SCAN)	5.45	98	4.1
Si (PBE)	5.48	89	4.2
Si (PBE+SCAN)	5.43	106	4.0
Si (PBE+r2SCAN)	5.45	97	4.1
Si (exp)	5.43	99	
NaCl (PBESOL)	5.60	26	4.7
NaCl (r2SCAN01)	5.63	26	4.9
NaCl (r2SCAN)	5.64	26	5.0
NaCl (PBE)	5.69	24	4.6
NaCl (PBE+r2SCAN)	5.61	27	4.9
NaCl (exp)	5.63	24	
Cu (PBESOL)	3.60	152	5.0
Cu (r2SCAN01)	3.61	146	5.0
Cu (r2SCAN)	3.61	146	5.0
Cu (exp)	3.61	137	

V. SUMMARY AND CONCLUSIONS

In this work we set out to adapt our PAW dataset generator software package ATOMPAW [19] to the meta-GGA functionals. In the course of this work, we found that several of the exchange-correlation functionals in the literature, including the r2SCAN functional of Furness *et al.* [15], are very sensitive to the electron number and kinetic energy densities. This observation motivated the development of a self-consistent solver algorithm based on cubic spline interpolation. The spline solver algorithm developed for use with the meta-GGA functionals appears to be more generally useful for finding self-consistent solutions to first- and second-order differential linear eigenvalue problems. One advantage of the spline solver method is its ability to ensure that the radial wave functions are smooth because of the cubic spline algorithm. Another advantage is that for each self-consistent iteration the needed one-electron energies and radial wave functions are found as solutions to an eigenvalue problem which, in our experience, converge very rapidly to the self-consistent solution.

From the converged all-electron atomic results, we have shown that the projector augmented-wave (PAW) construction methods can be adapted to produce consistent meta-GGA datasets. While fine tuning the dataset options and parameters for efficiency and accuracy will take more careful work, the preliminary results presented in Sec. IV are quite encouraging. Assessment of the advantages/disadvantages of constructing self-consistent datasets is still to be determined. In our limited study, we see differences in the binding-energy curves for r2SCAN and `PBE + r2SCAN` for NaCl, for example. On the other hand, the detailed analysis of the self-consistent electronic structure of spherical atoms with these meta-GGA functionals will hopefully be beneficial to future functional development. The implementations discussed in this paper are available in ATOMPAW version 4.2.0.0, which produces atomic datasets [39] in an XML format that is readable by several electronic structure codes.

ACKNOWLEDGMENTS

This work was supported by NSF Grant No. DMR-1940324. Computations were performed on the Wake Forest University DEAC cluster, a centrally managed resource with support provided in part by the university. Software assistance from Dr. Sean Anderson (DEAC Cluster administrator, Wake Forest University) is particularly appreciated. M.C. would like to acknowledge financial support by the Natural Sciences and Engineering Research Council of Canada (NSERC), under the Discovery Grants program Grant No. RGPIN-2016-06666. Susi Lehtola of the Molecular Sciences Software Institute (MoISSI) in Blacksburg, VA, provided valuable suggestions and also implemented the r2SCAN01 functional in the LIBXC library version 5.1.7. We would also like to thank John Perdew and Aaron Kaplan of Temple University, and James Furness and Jianwei Sun of Tulane University for helpful discussions and sharing of code. Helpful discussions with Grey Ballard of Wake Forest University are gratefully acknowledged. Early in the project, Surya Timilsina, currently at the University of Montréal, provided debugging assistance.

APPENDIX A: DETAILED EQUATIONS USED IN THE SPLINE SOLVER ALGORITHM

The derivation of Eq. (25) starts with mapping the radial grid with a logarithmic transformation of the form

$$r(u) = a_0(e^u - 1), \tag{A1}$$

where typically a_0 is taken as the value 0.1 Bohr. The differential eigenvalue problem of Eq. (20) can transformed to the variable u [where $0 \leqslant u \leqslant \ln(1 + r_{\max}/a_0)$] in terms of the function $Q(r(u))$, which is related to the radial wave function according to the following (suppressing the bound-state indices nl):

$$\varphi(r(u)) = e^{u/2}Q(r(u)). \tag{A2}$$

Here $r_{\max}$ denotes the radial range which in ATOMPAW is taken to be the fixed value $r_{\max} = 80$ Bohr. The differential equation for $Q(r(u))$ takes the form

$$A(u)\frac{d^2Q(r(u))}{du^2} + B(u)\frac{dQ(r(u))}{du} + V_Q(u)Q(u) = \varepsilon Q(u). \tag{A3}$$

Here

$$A(u) \equiv -\frac{[1 + V_\tau(r(u))]}{[r(u) + a_0]^2}, \tag{A4}$$

$$B(u) \equiv -\frac{1}{(r(u) + a_0)^2}\frac{dV_\tau(r(u))}{du}, \tag{A5}$$

$$\begin{aligned} V_Q(u) \equiv{}& [1 + V_\tau(r(u))]\frac{l(l+1)}{r(u)^2} \\ &+ \frac{dV_\tau(r)}{du}\left(\frac{1}{(r(u) + a_0)r(u)} - \frac{1}{2(r(u) + a_0)^2}\right) \\ &+ \frac{[1 + V_\tau(r(u))]}{4(r(u) + a_0)^2} + V_{\text{eff}}(r(u)). \end{aligned} \tag{A6}$$

Now the discretization of the radial points is accomplished by discretizing the variable u on a linear grid with step h and $u_k \equiv kh$. Here $k = 0, 1, 2, ...n_s$, but $k = 0$ is treated specially. The cubic spline interpolation can be formulated [30] in terms of the values of the function at the mesh points

$$Q_k \equiv Q(r(u_k)), \tag{A7}$$

and the second derivative of the function at the mesh points

$$M_k \equiv \frac{d^2Q(r(u_k))}{d^2u}. \tag{A8}$$

The first derivative of the function at each mesh point for $k > 0$ can be determined from the relation [30]

$$\frac{dQ(u_k)}{du} = \frac{Q_{k+1} - Q_k}{h} - (M_{k+1} + 2M_k)\frac{h}{6}. \tag{A9}$$

From these quantities and relationships, the differential equation (A3) evaluated on the mesh points for $k > 0$ can be written

$$A_kM_k + B_k\left(-\frac{h}{6}(M_{k+1} + 2M_k) + \frac{1}{h}(Q_{k+1} - Q_k)\right) + V_kQ_k = \varepsilon Q_k, \tag{A10}$$

where $V_k \equiv V_Q(r(u_k))$. This can be expressed in matrix form according to

$$\mathbf{\Omega}M + \mathbf{\Xi}Q = \varepsilon Q, \tag{A11}$$

where

$$\Omega_{jk} = (A_j - B_jh/3)\delta_{kj} - B_j(h/6)\delta_{k(j+1)}, \tag{A12}$$

and

$$\Xi_{jk} = (V_j - B_j/h)\delta_{kj} + (B_j/h)\delta_{k(j+1)}. \tag{A13}$$

As discussed in Sec. II A 3, the radial mesh points used for the eigenvalue equation excludes the origin and the index k takes the values $1, 2...n_s$. Typically, $n_s = 400$ is used. The cubic spline algorithm [30] includes a continuity condition for the slope of $Q(r(u))$ at all of the points $k > 0$ with the linear relation

$$\mathbf{F}M = \mathbf{G}Q, \tag{A14}$$

where $\mathbf{F}$ and $\mathbf{G}$ are $n_s \times n_s$ tridiagonal matrices and M and Q are both vectors of length n_s, representing the second derivative and function values at the interior mesh points:

$$\mathbf{F} = \begin{pmatrix} a_1 & b_1 & 0 & \cdots & 0 \\ c_2 & a_2 & b_2 & \cdots & 0 \\ \vdots & \vdots & \vdots & \vdots & b_{n_s-1} \\ 0 & 0 & 0 & c_{n_s-1} & a_{n_s} \end{pmatrix} \tag{A15}$$

and

$$\mathbf{G} = \frac{3}{h^2}\begin{pmatrix} \alpha_1 & \beta_1 & 0 & \cdots & 0 \\ \gamma_2 & \alpha_2 & \beta_2 & \cdots & 0 \\ \vdots & \vdots & \vdots & \vdots & \beta_{n_s-1} \\ 0 & 0 & 0 & \gamma_{n_s-1} & \alpha_{n_s} \end{pmatrix}. \tag{A16}$$

The coefficients for $i \geqslant 2$ are given by [30]

$$a_i = 2, \quad b_i = c_i = 1/2, \quad \alpha_i = -2, \quad \beta_i = \gamma_i = 1. \tag{A17}$$

For the mesh point $k = 1$, the slope condition is altered by the fact that the differential equation near the origin requires that for some constants q_0 and q_1,

$$Q(u) \approx q_0u^{l+1} + q_1u^{l+2}. \tag{A18}$$

This determines the values of Eq. (A14) for the $i = 1$ row as

$$a_1 = (2l + 5)/[2(l + 1)] \quad b_1 = 1/2;$$
$$\alpha_1 = -(l + 4)/2 \quad \beta_1 = 1. \tag{A19}$$

These results can be combined in order to evaluate the form of $\mathbf{\Lambda}$ in Eq. (25) as

$$\mathbf{\Lambda} = \mathbf{\Omega}(\mathbf{F}^{-1}\mathbf{G}) + \mathbf{\Xi}. \tag{A20}$$

Interestingly, although $\mathbf{\Lambda}$ is a full nonsymmetric matrix, it is our experience that the needed eigenvalues ε_{nl} are real.

From the solution of the linear eigenvalue problem Eq. (25), we now know the values of Q_k for $0 \leqslant k \leqslant n_s$ since $Q_0 = 0$. We also can determine M_k for $1 \leqslant k \leqslant n_s$ from Eq. (A14). From the known behavior of the wave function near the origin [Eq. (A18)], we also know that $M_0 = 0$ for $l \geqslant 2$. It can be shown that for $l = 0$,

$$M_0 = \frac{1}{A_0 - B_0h/3}\left\{B_0\left(\frac{M_1h}{6} - \frac{Q_1}{h}\right) + \left(-\frac{1}{a_0}\frac{dV_\tau(0)}{du} - (rV_{\text{eff}}(r))_{r\to 0}\right)\left(\frac{Q(r(u))}{r(u)}\right)_{r\to 0}\right\}. \tag{A21}$$

For $l = 1$ we have

$$M_0 = \frac{1}{A_0 - B_0h/3}\left\{B_0\left(\frac{M_1h}{6} - \frac{Q_1}{h}\right) - 2(1 + V_\tau(0))\left(\frac{Q(r(u))}{(r(u))^2}\right)_{r\to 0}\right\}. \tag{A22}$$

From these values of Q_k and M_k, we can evaluate the radial wave function and its second derivative on the mesh points:

$$\varphi(r_k) \equiv \varphi_k = Q_ke^{u_k/2}, \tag{A23}$$

$$M^\varphi(r_k) \equiv \frac{d^2\varphi(r_k)}{dr^2} \equiv M_k^\varphi = \frac{e^{u_k/2}}{(r(u_k) + a_0)^2}\left(M_k - \frac{1}{4}Q_k\right). \tag{A24}$$

Now, from the knowledge of these values on the mesh points, we can use the cubic spline analysis [31] to interpolate the radial wave function on the grid points of the rest of the calculation. For $r_i \leqslant r < r_{i+1}$ and $\xi \equiv r - r_i$,

$$\varphi(r) = C_1^i + \xi C_2^i + \tfrac{1}{2}\xi^2C_3^i + \tfrac{1}{6}\xi^3C_4^i. \tag{A25}$$

The coefficients defined by de Boor [31] are related to the values and second derivatives and the increment values $h_{i+1} \equiv r_{i+1} - r_i$ according to

$$C_1^i = \varphi_i$$
$$C_2^i = \left(\frac{\varphi_{i+1} - \varphi_i}{h_{i+1}} - \left(M_{i+1}^\varphi + 2M_i^\varphi\right)\frac{h_{i+1}}{6}\right)$$
$$C_3^i = M_i^\varphi$$
$$C_4^i = \frac{M_{i+1}^\varphi - M_i^\varphi}{h_{i+1}}. \tag{A26}$$

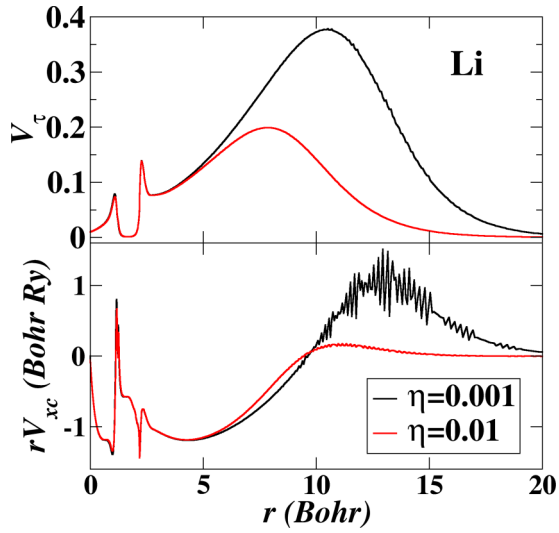

FIG. 13. Comparison of the self-consistent radial potentials $rV_{xc}(r)$ and $V_\tau(r)$ for Li using the r2SCAN functional with $\eta = 0.01$ and $\eta = 0.001$. For this case, $n_s = 400$ was used.

Some other details of the implementation of the spline solver include the observation that the scheme also works quite efficiently for cases in which $V_\tau(r) \equiv 0$, with results very close to those obtained with finite-difference analysis. For this case ATOMPAW uses the finite-difference algorithms by default, but the keyword "splineinterp" on the second line of the input file activates the spline solver algorithm. For $V_\tau(r) \neq 0$ ATOMPAW automatically uses the spline solver algorithm to find the self-consistent bound states. We find that additional care needs be taken in order to accommodate the sensitive dependence on the functional to $n(r)$ and $\tau(r)$. For example, the code first finds the self-consistent solution using the local density approximation (LDA) for the exchange-correlation functional [32] in order generate reasonable initial values of $n(r)$ and $\tau(r)$. For converging the MGGA equations, self-consistency is achieved by iterating the $n(r)$ rather than iterating Kohn-Sham potential as is usually done. Additionally, intermediate evaluations of $V_\tau(r)$ and $V_{xc}(r)$ are performed on a fine linear grid to improve the accuracy within the self-consistent iterations.

In order to illustrate the sensitivity of the $V_{xc}(r)$ and $V_\tau(r)$ functions for atoms in the first two columns of the periodic table, Fig. 13 shows a plot of these potentials for Li, evaluated for $n_s = 400$, analogous to Fig. 2 which was evaluated with $n_s = 2000$. The rapid oscillations in $V_{xc}(r)$ for $r > 10$ Bohr for the $\eta = 0.001$ case do not affect the physical properties of the results. For example, the total atomic energy computed with $n_s = 400$ and $n_s = 2000$ for a Li atom with the r2SCAN $\eta = 0.001$ functional differs by less than 1×10^{-6} Ry.

APPENDIX B: DETAILS FOR SOLVING THE RADIAL PAW EQUATIONS FOR THE GENERALIZED KOHN-SHAM EQUATIONS

The evaluation of the PAW formulation for the generalized Kohn-Sham equations introduces minor changes. In order not to confuse the solutions for the radial functions from the basis functions, we will use the notation $\tilde{\psi}_{\varepsilon l}(r)$ and $\psi_{\varepsilon l}(r)$ for the pseudo and all-electron functions for one-electron energy ε and angular momentum quantum number l. The complex indices $n_i l_i m_i$ used for the basis and projector functions will be contracted to just i with the understanding that all matrix elements are diagonal in angular momentum quantum numbers. For a pseudo wave function $\tilde{\psi}_{\varepsilon l}(r)$, these equations take the form

$$[\mathbf{H}^{\mathrm{PAW}}(r) - \varepsilon \mathbf{O}^{\mathrm{PAW}}]\tilde{\psi}_{\varepsilon l}(r) = 0. \tag{B1}$$

Here

$$\mathbf{H}^{\mathrm{PAW}}(r) = \tilde{H}(r) + \sum_{a,i,j} |\tilde{p}_i^a\rangle D_{ij}^a \langle \tilde{p}_j^a|, \tag{B2}$$

where from the constructed basis and projector functions, the matrix elements are diagonal for the angular momentum quantum number l_i and are evaluated as follows:

$$D_{ij}^a = \langle \varphi_{n_i l_i}^a | H^a(r) | \varphi_{n_j l_i}^a \rangle - \langle \tilde{\varphi}_{n_i l_i}^a | \tilde{H}^a(r) | \tilde{\varphi}_{n_j l_i}^a \rangle. \tag{B3}$$

The overlap operator is given by

$$\mathbf{O}^{\mathrm{PAW}} = \mathbf{1} + \sum_{a,i,j} |\tilde{p}_i^a\rangle O_{ij}^a \langle \tilde{p}_j^a|, \tag{B4}$$

where

$$O_{ij}^a = \langle \varphi_{n_i l_i}^a | \varphi_{n_j l_i}^a \rangle - \langle \tilde{\varphi}_{n_i l_i}^a | \tilde{\varphi}_{n_j l_i}^a \rangle. \tag{B5}$$

In these expressions, $H(r)$ and $\tilde{H}(r)$ are given by Eqs. (21) and (48), respectively. The solution of Eq. (B1) can be performed by slightly modifying the procedure introduced by Blöchl [18], performed for each angular momentum channel l:

$$\tilde{\psi}_{\varepsilon l}(r) = \tilde{\psi}_{\varepsilon l}^0(r) + \sum_k C_k \tilde{\psi}_{\varepsilon l}^k(r), \tag{B6}$$

where

$$(\tilde{H} - \varepsilon)\tilde{\psi}_{\varepsilon l}^0(r) = 0, \tag{B7}$$

and

$$(\tilde{H} - \varepsilon)\tilde{\psi}_{\varepsilon l}^k(r) = \tilde{p}_k(r). \tag{B8}$$

Equation (B7) can be solved using the same method [29] as described for solving Eq. (24). This method can be also adapted to solve the inhomogeneous differential equations (B8). With these solutions, the coefficients $\{C_k\}$ can be determined by solving the linear equations

$$C_k + \sum_{m,n} (D_{km} - \varepsilon O_{km}) \langle \tilde{p}_m | \tilde{\psi}_{\varepsilon l}^n \rangle C_n + \sum_m (D_{km} - \varepsilon O_{km}) \langle \tilde{p}_m | \tilde{\psi}_{\varepsilon l}^0 \rangle = 0. \tag{B9}$$

Since the range of the projector functions $\tilde{p}_k(r)$ is confined within the augmentation sphere, Eqs. (B7) and (B8) need to be evaluated only within the augmentation sphere. In fact, since ε is not necessarily a bound-state eigenvalue, the long-range

behavior of $\tilde{\psi}_{\varepsilon l}(r)$ is not well defined. From these results for the pseudo wave functions $\tilde{\psi}_{\varepsilon l}(r)$ we can also approximate the corresponding all-electron function by using the PAW transformation:

$$\psi_{\varepsilon l}(r) \approx \tilde{\psi}_{\varepsilon l}(r) + \sum_j (\varphi_j(r) - \tilde{\varphi}_j(r))\langle \tilde{p}_j | \tilde{\psi}_{\varepsilon l}\rangle. \quad \text{(B10)}$$

This form restores the correct nodal behavior of the all-electron functions within the augmentation sphere. These results can be used to estimate the logarithmic derivatives as a function of energy ε compared with the all-electron logarithmic derivatives calculated directly, as was needed to construct Fig. 11.

[1] P. Hohenberg and W. Kohn, Phys. Rev. **136**, B864 (1964).
[2] W. Kohn and L. J. Sham, Phys. Rev. **140**, A1133 (1965).
[3] Z.-H. Yang, H. Peng, J. Sun, and J. P. Perdew, Phys. Rev. B **93**, 205205 (2016).
[4] J. Sun, A. Ruzsinszky, and J. P. Perdew, Phys. Rev. Lett. **115**, 036402 (2015).
[5] J. H. Yang, D. A. Kitchaev, and G. Ceder, Phys. Rev. B **100**, 035132 (2019).
[6] F. Tran, J. Doumont, P. Blaha, M. A. L. Marques, S. Botti, and A. P. Bartók, J. Chem. Phys. **151**, 161102 (2019).
[7] P. Kovács, F. Tran, P. Blaha, and G. K. H. Madsen, J. Chem. Phys. **150**, 164119 (2019).
[8] A. Chakraborty, M. Dixit, D. Aurbach, and D. T. Major, npj Comput. Mater. **4**, 60 (2018).
[9] S. Jana, K. Sharma, and P. Samal, J. Chem. Phys. **149**, 164703 (2018).
[10] Y. Zhang, D. A. Kitchaev, J. Yang, T. Chen, S. T. Dacek, R. A. Sarmiento-Pérez, M. A. L. Marques, H. Peng, G. Ceder, J. P. Perdew, and J. Sun, npj Comput. Mater. **4**, 9 (2018).
[11] C. Shahi, J. Sun, and J. P. Perdew, Phys. Rev. B **97**, 094111 (2018).
[12] E. B. Isaacs and C. Wolverton, Phys. Rev. Mater. **2**, 063801 (2018).
[13] I. G. Buda, C. Lane, B. Barbiellini, A. Ruzsinszky, J. Sun, and A. Bansil, Sci. Rep. **7**, 44766 (2017).
[14] A. P. Bartók and J. R. Yates, J. Chem. Phys. **150**, 161101 (2019).
[15] J. W. Furness, A. D. Kaplan, J. Ning, J. P. Perdew, and J. Sun, J. Phys. Chem. Lett. **11**, 8208 (2020).
[16] J. Sun, M. Marsman, G. I. Csonka, A. Ruzsinszky, P. Hao, Y.-S. Kim, G. Kresse, and J. P. Perdew, Phys. Rev. B **84**, 035117 (2011).
[17] Y. Yao and Y. Kanai, J. Chem. Phys. **146**, 224105 (2017).
[18] P. E. Blöchl, Phys. Rev. B **50**, 17953 (1994).
[19] N. A. W. Holzwarth, A. R. Tackett, and G. E. Matthews, Comput. Phys. Commun. **135**, 329 (2001), available from the website http://pwpaw.wfu.edu.
[20] X. Gonze, B. Amadon, G. Antonius, F. Arnardi, L. Baguet, J.-M. Beuken, J. Bieder, F. Bottin, J. Bouchet, E. Bousquet, N. Brouwer, F. Bruneval, G. Brunin, T. Cavignac, J.-B. Charraud, W. Chen, M. Côté, S. Cottenier, J. Denier, G. Geneste *et al.*, Comput. Phys. Commun. **248**, 107042 (2020).
[21] P. Giannozzi, O. Baseggio, P. Bonfà, D. Brunato, R. Car, I. Carnimeo, C. Cavazzoni, S. de Gironcoli, P. Delugas, F. Ferrari Ruffino, A. Ferretti, N. Marzari, I. Timrov, A. Urru, and S. Baroni, J. Chem. Phys. **152**, 154105 (2020).
[22] Jean-Baptiste Charraud and Marc Torrent have implemented the capability of treating meta-GGA functionals within ABINIT Version 9.6, available from the website https://www.abinit.org/. Some details of the implementation are described in the Ph.D. thesis cited in Ref. [[51] online].
[23] See Supplemental Material at http://link.aps.org/supplemental/10.1103/PhysRevB.105.125144 for sample inputs to ATOMPAW and ABINIT.
[24] M. A. Marques, M. J. Oliveira, and T. Burnus, Comput. Phys. Commun. **183**, 2272 (2012).
[25] S. Lehtola, C. Steigemann, M. J. Oliveira, and M. A. Marques, SoftwareX **7**, 1 (2018).
[26] This paper is focused on preparing atomic datasets for use in codes which model materials. It is assumed that the prepared datasets are capable of properly representing spin effects within these material codes such as ABINIT [20] and QUANTUM ESPRESSO [21].
[27] In Ref. [25], the symbol γ is used instead of σ.
[28] D. R. Hartree, *The Calculation of Atomic Structures* (John Wiley and Sons, Inc., New York, 1957).
[29] For example, ATOMPAW makes use of the cfdsol subroutine, which is based on a high-order predictor-corrector algorithm. The code was borrowed from the Ultra Soft Pseudopotential code described in Ref. [45].
[30] J. H. Ahlberg, E. N. Nilson, and J. L. Walsh, *The Theory of Splines and Their Application* (Academic Press, Inc., New York, 1967).
[31] C. de Boor, *A Practical Guide to Splines* (Springer-Verlag, New York, 1978).
[32] J. P. Perdew and Y. Wang, Phys. Rev. B **45**, 13244 (1992).
[33] J. P. Perdew, K. Burke, and M. Ernzerhof, Phys. Rev. Lett. **77**, 3865 (1996); **78**, 1396(E) (1997).
[34] N. A. W. Holzwarth, G. E. Matthews, R. B. Dunning, A. R. Tackett, and Y. Zeng, Phys. Rev. B **55**, 2005 (1997).
[35] G. Kresse and D. Joubert, Phys. Rev. B **59**, 1758 (1999).
[36] A. R. Tackett, N. A. W. Holzwarth, and G. E. Matthews, Comput. Phys. Commun. **135**, 348 (2001).
[37] M. Torrent, F. Jollet, F. Bottin, G. Zérah, and X. Gonze, Comput. Mater. Sci. **42**, 337 (2008).
[38] M. Torrent, N. A. W. Holzwarth, F. Jollet, D. Harris, N. Lepley, and X. Xu, Comput. Phys. Commun. **181**, 1862 (2010).
[39] F. Jollet, M. Torrent, and N. Holzwarth, Comput. Phys. Commun. **185**, 1246 (2014).
[40] A. Martin, M. Torrent, and R. Caracas, Phys. Rev. B **99**, 094112 (2019).
[41] N. A. W. Holzwarth, Comput. Phys. Commun. **243**, 25 (2019).
[42] M. Marsman and G. Kresse, J. Chem. Phys. **125**, 104101 (2006).
[43] U. von Barth and C. D. Gelatt, Phys. Rev. B **21**, 2222 (1980).
[44] S. G. Louie, S. Froyen, and M. L. Cohen, Phys. Rev. B **26**, 1738 (1982).
[45] D. Vanderbilt, Phys. Rev. B **41**, 7892 (1990), USPP code is available from the website http://www.physics.rutgers.edu/~dhv/uspp/.

[46] D. R. Hamann, M. Schlüter, and C. Chiang, Phys. Rev. Lett. **43**, 1494 (1979).
[47] G. P. Kerker, J. Phys. C: Solid State Phys. **13**, L189 (1980).
[48] N. Troullier and J. L. Martins, Phys. Rev. B **43**, 1993 (1991).
[49] C. Brock, A. Tackett, and D. Walker, Comput. Phys. Commun. **247**, 106929 (2020).
[50] X. Gonze, P. Käckell, and M. Scheffler, Phys. Rev. B **41**, 12264 (1990).
[51] J.-B. Charraud, Studies of superhydrides by ab-initio and machine learning accelerated random structure searching, Ph.D. thesis, Université Paris-Saclay, 2021, available from the website https://hal.archives-ouvertes.fr/tel-03405328/.
[52] J. P. Perdew, A. Ruzsinszky, G. I. Csonka, O. A. Vydrov, G. E. Scuseria, L. A. Constantin, X. Zhou, and K. Burke, Phys. Rev. Lett. **100**, 136406 (2008).
[53] F. Birch, Phys. Rev. **71**, 809 (1947), quoted in Wikipedia article https://en.wikipedia.org/wiki/Birch-Murnaghan_equation_of_state.
[54] C. Kittel, *Introduction to Solid State Physics*, 7th ed. (John Wiley and Sons, Inc., New York, 1996).